

Using Objective Analysis of Scanning Radiometer Measurements to Compute the Water Vapor Path Delay for Altimetry

Jacques Stum, Philippe Sicard, Loren Carrère, and Juliette Lambin

Abstract—An objective analysis (OA) method is implemented to compute the water vapor path delay (PD) correction of the altimeter range using total precipitable water measurements from scanning microwave radiometers (Advanced Microwave Sounding Unit A, Advanced Microwave Scanning Radiometer-Earth Observing System, Tropical Rain Measuring Mission Microwave Imager, and Special Sensor Microwave Imager). The European Centre for Medium Range Weather Forecasts (ECMWF) model-derived water vapor PD correction given in the altimeter products is used as the first-guess field. The calculation of the statistical variables required by the OA is presented: These include the variance and correlation function of the radiometer observations minus its first guess, as well as the observation error variance. The performance of the OA-derived water vapor PD correction is assessed, using four months of Jason-1 altimeter data. It is shown that the OA-derived correction is more accurate than the ECMWF-derived correction but remains less accurate than the one derived from the Jason microwave radiometer.

Index Terms—Altimetry, ECMWF, objective analysis, water vapor path delay.

I. INTRODUCTION

PERMANENT gases in the atmosphere induce propagation delay to pulses emitted by satellite-borne radar altimeters to the ocean surface: The range measurement has to be corrected for this effect. The range correction due to water vapor has been called “wet tropospheric correction” or “path delay” (hereafter referred to as PD). It varies from 1 cm in dry cold air to 40 cm in wet hot air and is highly variable in space and time. It has long been recognized that the most accurate way to measure it is to fly a microwave radiometer together with the radar altimeter, sensing the atmosphere at frequencies near the 22.235-GHz water vapor absorption line, along the altimeter path (i.e., nadir viewing). A second possibility is to compute the PD from meteorological models but with poorer accuracy because such models often cannot

map the atmospheric humidity short space and timescales [1]. In this paper, an alternate approach is proposed which combines, through an objective analysis (OA) method, all existing scanning radiometer columnar water vapor observations to derive the PD for any altimeter mission. This paper is motivated by the need to offer an improved PD correction, the main interest being for altimeter missions that do not embark a microwave radiometer. This alternate PD correction may also benefit the sea level rise studies using altimeter missions for which the long term stabilities of both the aboard radiometer PD and the model PD are uncertain. First, the scanning radiometer measurements used are assessed in Section II. Section III describes the OA method. Finally, Section IV is devoted to the method validation with a four-month Jason-1 altimeter data set.

II. DESCRIPTION OF THE SCANNING RADIOMETER MEASUREMENTS

A. Satellites and Sensors

Total precipitable water measurements are made by several existing scanning radiometers on board a variety of satellite platforms for meteorological operational applications or water cycle research. These are the Advanced Microwave Sounding Unit A (AMSU-A) sensor on board the National Oceanic and Atmospheric Administration (NOAA) satellite series or on board the European Organisation for the Exploitation of Meteorological Satellites MetOp-A satellite, the Special Sensor Microwave Imager (SSM/I) sensor on board the Defense Meteorological Satellite Program (DMSP) satellite series, the Advanced Microwave Scanning Radiometer-Earth Observing System (AMSR-E) sensor on board the National Aeronautics Space Administration (NASA) Aqua satellite, and the Tropical Rain Measuring Mission (TRMM) Microwave Imager (TMI) on board the joint NASA and Japan Aerospace Exploration Agency TRMM satellite.

B. Product Data Set

For the needs of this paper, a one-year 2008 data set has been used, built from five AMSU-A sensors (flying on board the NOAA-15, NOAA-16, NOAA-17, NOAA-18, and MetOp-A), the SSM/I sensor on board the DMSP-F13, the AMSR-E, and the TMI. Level-2 swath products from these sensors all contain the total precipitable water together with the pixel latitude, longitude, and time. Pixel quality flags are

Manuscript received July 15, 2010; revised November 12, 2010; accepted December 15, 2010. Date of publication February 10, 2011; date of current version August 26, 2011.

J. Stum, P. Sicard, and L. Carrère are with the Collecte Localisation Satellites, 31526 Ramonville, France (e-mail: jstum@cls.fr).

J. Lambin is with the Centre National d'Etudes Spatiales, 31400 Toulouse, France.

Color versions of one or more of the figures in this paper are available online at <http://ieeexplore.ieee.org>.

Digital Object Identifier 10.1109/TGRS.2011.2104967

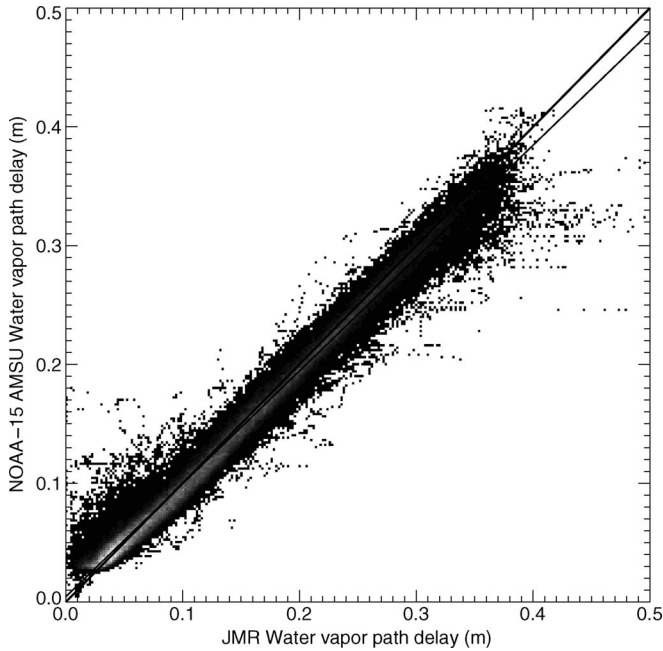


Fig. 1. Scatter plot of NOAA-15 AMSU-A versus JMR PD (in meters). Gray tones denote the concentration of the samples from (black) low to (white) high.

also given for some of them (e.g., AMSR-E) and are useful to edit data contaminated by rain or sea ice. The pixels are provided every 10 km for the AMSR-E and the TMI, every 25 km for the SSMI, and every 50 km for the AMSU-A (at the swath middle). For the AMSU-A and the SSMI, these level-2 products have been made available by the NOAA through its Comprehensive Large Array-Data Stewardship System (CLASS). For the AMSU-A and the SSMI, these level-2 products have been made available by the NOAA through its Comprehensive Large Array-Data Stewardship System (CLASS). For the AMSR-E, the level-2 product data set was downloaded from the National Snow and Ice Data Center (ftp://n4ftl01u.ecs.nasa.gov/SAN/AMSA/AE_Ocean.002/), and for the TMI, the level-2 product data set was acquired from the Global Hydrology Resource Center (<ftp://ghrc.nsstc.nasa.gov/pub2/data/tmi-op/2008/>).

C. Calculation of PD From Total Precipitable Water

The total precipitable water content W in centimeters is given by

$$W = \int_0^H \rho_v dz \quad (1)$$

where ρ_v is the water vapor density in grams per cubic centimeter, z is the altitude, and H is the altitude above which the water vapor density is considered to be negligible.

The water vapor PD correction can be approximated by [2]

$$PD = 1763 \int_0^H \frac{\rho_v}{T} dz \quad (2)$$

where PD is in centimeters and T is the temperature in kelvin.

The ratio between PD and W can be described by a decreasing function of water vapor content (e.g., see Fig. 1 in [3]), which expresses its temperature dependence. In this paper, the

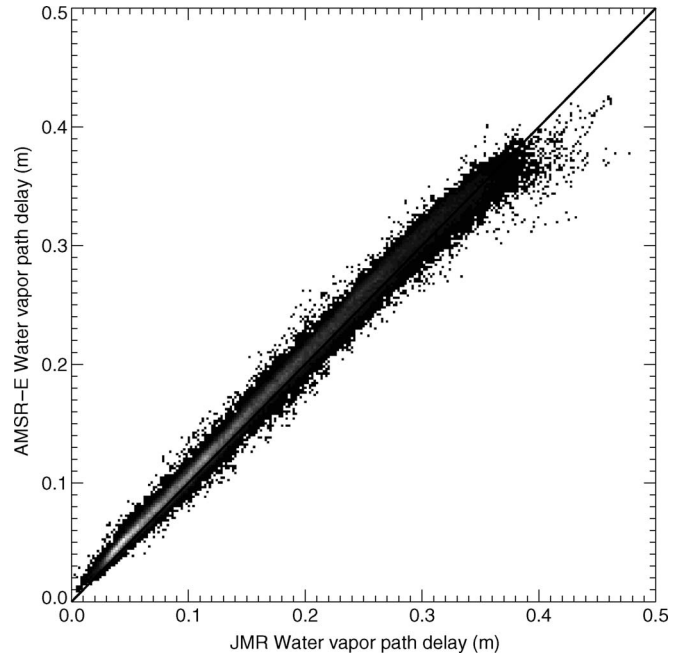


Fig. 2. Scatter plot of the AMSR-E versus JMR PD (in meters). Gray tones denote the concentration of the samples from (black) low to (white) high.

temperature and humidity profiles from the European Centre for Medium Range Weather Forecasts (ECMWF) model outputs were used to derive the following function to calculate PD from W :

$$PD/W = a_0 + a_1W + a_2W^2 + a_3W^3 \quad (3)$$

with $a_0 = 6.8544$, $a_1 = -0.4377$, $a_2 = 0.0714$, and $a_3 = -0.0038$.

This function gives PD values about 1% lower than those derived from the function given in [3], with a PD/W ratio of 6.48 for $W = 1$ cm and 5.97 for $W = 6$ cm.

D. Comparison of the Water Vapor PDs of the Different Sensors

As the goal of this paper is to combine the PDs from the different sensors, it is thus necessary to estimate their errors and correct for possible biases before using it in the OA. The Jason-1 Microwave Radiometer (JMR) is used as a common reference for the comparison. The first four months of 2008, corresponding to Jason-1 cycles 221 to 232, have been used to compute the PD from each scanning radiometer at the time and location of the altimeter measurements, using bilinear interpolation from the four closest surrounding pixels and selecting only the scan times less than half an hour apart from the altimeter time. Only good quality JMR measurements (edited for rain and ice contamination) are kept. The obtained scatter plots of the NOAA-15 AMSU-A, AMSR-E, TMI, and SSMI versus JMR PD are shown in Figs. 1–4, respectively, and Table I summarizes the statistics for all sensors. There is more scatter for the AMSU-A than for the other sensors (the standard deviation is about 12 mm). This may be explained by the less accurate total water vapor contents because of the lack of a low-frequency channel (around 18 GHz) to estimate the contribution of the surface wind-induced emissivity variation in the water

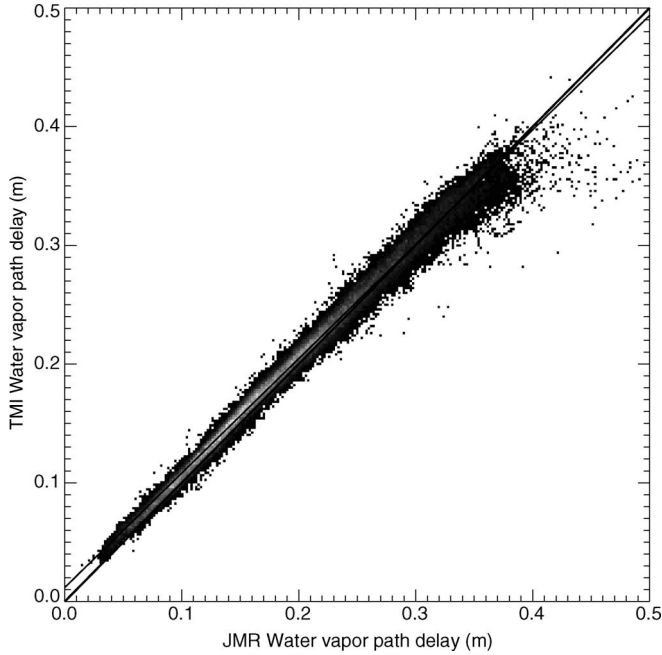


Fig. 3. Scatter plot of the TMI versus JMR PD (in meters). Gray tones denote the concentration of the samples from (black) low to (white) high.

vapor retrieval. It also may be explained by the coarse AMSU-A pixel resolution (~ 50 km at the nadir and more than 100 km at the swath edge). Not shown here are the other AMSU-A scatter plots, but the same conclusions can be derived. In particular, some increased scatter is observed for the NOAA-17 AMSU-A for low PD values, which may be due to the loss of the 86-GHz channel used to edit pixels contaminated by sea ice. Among all these five AMSU-A sensors, the most accurate one seems to be the one aboard MetOp-A (see Table I). It is also remarkable to see the good intercalibration of these sensors (no bias observed). By contrast, Fig. 4 shows that the SSMI on F13 is clearly overestimating the PD by $\sim 10\%$. The most accurate sensors are the AMSR-E and the TMI (see Figs. 2 and 3). In particular, the agreement between the AMSR-E and JMR PDs is excellent, with no bias, and has a standard deviation of about 7 mm.

To build a more homogenous multisensor PD data set, each sensor has then been corrected using the a and b values of Table I

$$\text{correctedPD} = (1/a)(\text{PD} - b). \quad (4)$$

III. OBJECTIVE ANALYSIS

OA was introduced in oceanography by Bretherton *et al.* [4] and has been widely used for the global mapping of different oceanic variables, like sea surface temperature [5], sea level anomalies [6], or phytoplankton concentration [7]. Its purpose is to estimate the value of a field F at a given point P , starting from a first-guess value G and using N measurements of the field made at different locations and times in the vicinity of point P

$$F(P) = G(P) + \sum_{i=1}^N W_i \text{Anom}_i. \quad (5)$$

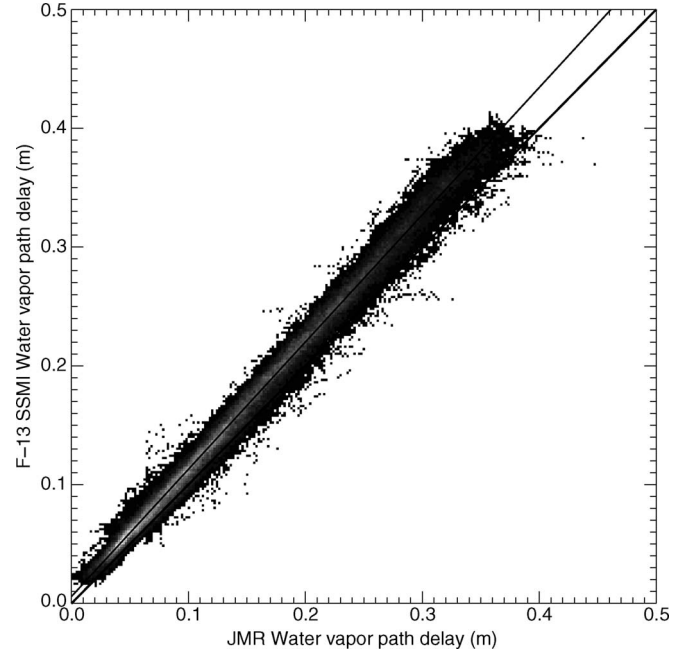


Fig. 4. Scatter plot of the F-13 SSMI versus JMR PD (in meters). Gray tones denote the concentration of the samples from (black) low to (white) high.

In (5), Anom_i is the field anomaly, i.e., the difference between the field measurement F_i and the first-guess value $G(P)$

$$\text{Anom}_i = F_i - G(P). \quad (6)$$

In this paper, the field measurements F_i are the sensor PD measurements, and we chose for the first-guess value $G(P)$ the PD derived from the ECMWF model analysis. This choice will be discussed further on. The anomalies are thus the (sensor-ECMWF) PD differences.

W_i denotes the weights, built using *a priori* knowledge of the statistical properties of the anomalies and of the measurement errors

$$W_i = \sum_{j=1}^N C_j A_{ij}^{-1}. \quad (7)$$

In (7), C_j is the covariance of the anomaly between point j , which is some distance and time away from point P , and point P where the estimation is done

$$C_j = \frac{\text{CorAno}(j, P) \sqrt{\text{VarAno}(j) \text{VarAno}(P)}}{\text{VarAno}(P)} \quad (8)$$

where $\text{CorAno}(j, P)$ is the space and time correlation coefficient of the anomaly between point j , which is some distance and time away from point P , and point P . VarAno denotes the variance of the field of the PD anomaly (the signal variance). The closer in space and time a measurement from point P is, the higher is its weight W_i .

In (7), A_{ij} ($= A_{ji}$) denotes the variance-covariance matrix of the anomalies, and A_{ij}^{-1} is its inverse matrix. The diagonal terms A_{ii} and nondiagonal terms A_{ij} for $i \neq j$ are computed as follows:

$$A_{ii} = \frac{\text{VarErr}(i) + \text{VarAno}(i)}{\text{VarAno}(P)} \quad (9)$$

TABLE I
 STATISTICS OF (SENSOR-JMR) PD DIFFERENCE: NUMBER OF SAMPLES, MEAN, STANDARD DEVIATION IN CENTIMETERS, SLOPE a , AND INTERCEPT b OF THE LINEAR REGRESSION LINE $(SensorPD) = a \times (JMRPD) + b$ WITH PD AND b IN CENTIMETERS

Sensor	Nsamples	Mean	stdev	a	b
AMSU-15	281840	-0.2	1.2	0.95	0.04
AMSU-16	290081	-0.3	1.2	0.95	0.3
AMSU-17	288211	0.0	1.1	0.98	0.2
AMSU-18	300658	-0.1	1.1	0.96	0.4
AMSU-MA	268017	-0.1	0.97	0.97	0.2
SSMI F13	155961	1.7	1.1	1.07	1.6
TMI	87218	0.5	0.9	0.96	1.0
AMSR-E	168563	0.6	0.7	0.99	0.0

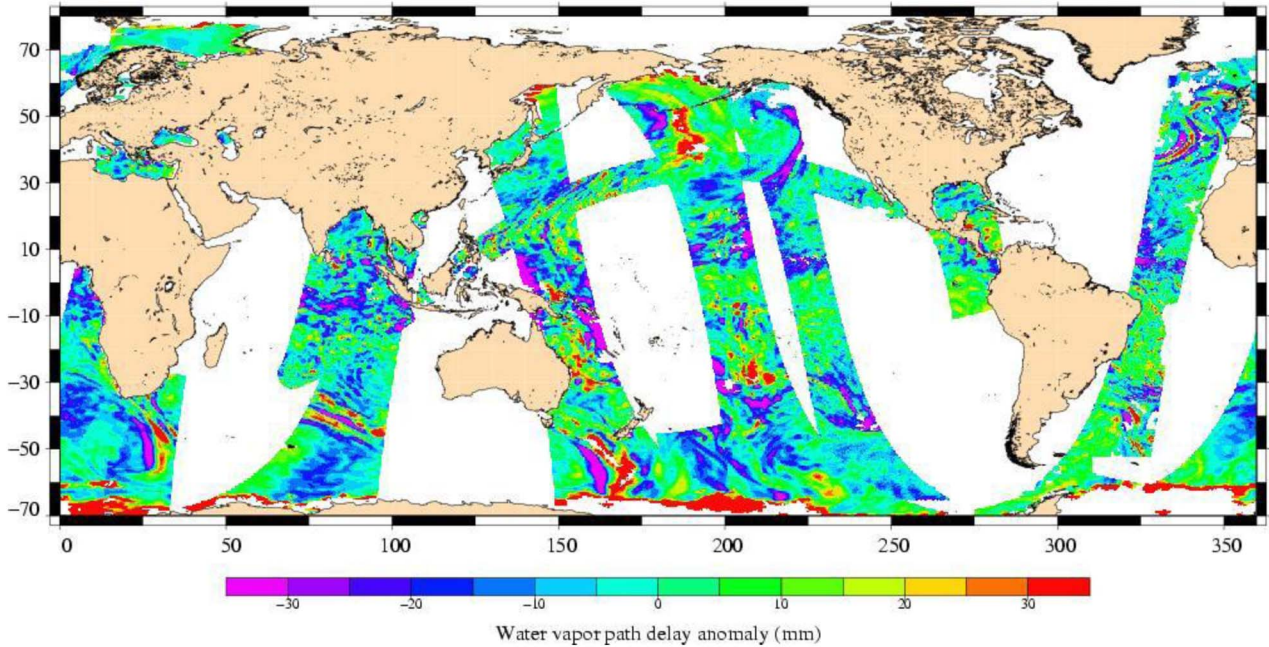


Fig. 5. Hourly PD anomaly map for January 1, 2008, built from eight sensors. Color scale is from (left) -30 mm to (right) +30 mm.

where $VarErr$ is the variance of the measurement error

$$A_{ij} = \frac{CorAno(i, j) \sqrt{VarAno(i) VarAno(j)}}{VarAno(P)}. \quad (10)$$

In (8)–(10), the variances and covariances are normalized with respect to the signal variance at point P .

Associated to the estimated value $F(P)$ given by (5) is the estimation formal error variance $E(P)$ given here normalized with respect to the signal variance

$$E(P) = 1 - \sum_{i=1}^N \sum_{j=1}^N C_i C_j A_{ij}^{-1}. \quad (11)$$

$E(P)$ is thus a dimensionless quality indicator of the estimated value $F(P)$. It tends to zero when measurements are

available close in space and time from point P ; it is one when no measurements are available at all.

Four quantities are thus needed to compute $F(P)$:

- 1) the first-guess value $G(P)$;
- 2) the variance of the measurement error $VarErr$;
- 3) the signal variance $VarAno$;
- 4) the correlation function of the field of the PD anomaly $CorAno$.

A. Choice of the First Guess

The ECMWF water vapor PD given in the altimeter Geophysical Data Records (GDR) is used as the first-guess field. The main interest in choosing this first guess is to ensure the computation of a seamless PD correction for every altimetric measurement. Indeed, when sensor observations are not close

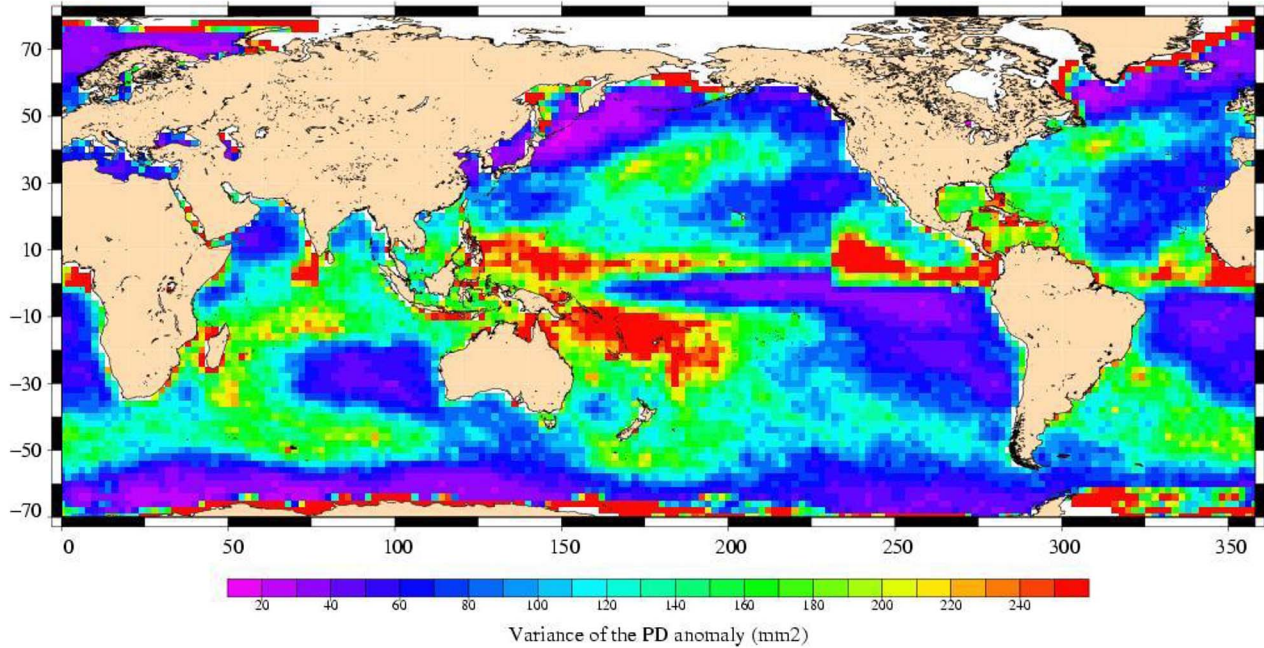


Fig. 6. January mean of the 12-h variance of the water vapor PD anomaly. Color scale is from (left) 20 mm² to (right) 250 mm².

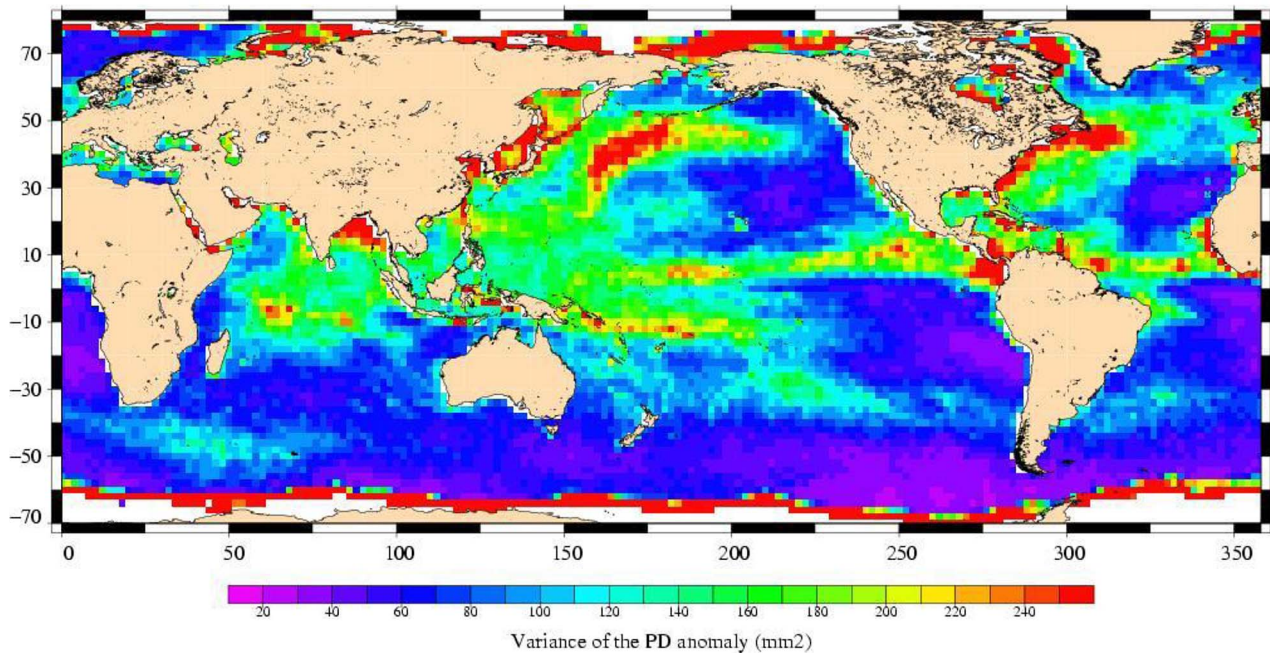


Fig. 7. Same as Fig. 6 except that it is for July.

enough in space or time to the altimeter point, the weights in (5) tend to zero, and the returned value $F(P)$ tends to $G(P)$. In the altimeter GDR, the ECMWF PD $G(P)$ is provided at the time and location of the altimeter measurement by the interpolation in the ECMWF Gaussian (native) grids (spatial resolution of about 25 km) provided every 6 h by the French Met Office, Météo-France.

B. Variance of the Measurement Error

The estimation of the accuracy of the water vapor content retrieved by a spaceborne radiometer is difficult to achieve due

to the lack of accurate reference measurements. Radiosonde observations have long been used as “ground truth” but suffer from their own inaccuracies and limited number over ocean. For example, Brown *et al.* [8] only found 38 coincident radiosonde samples within 75 km and 1 h from the JMR over an ~ 1 -year time period. In this paper, the square of the (sensor–JMR) standard deviation reported in Table I has been taken as a preliminary estimate of the variance of the measurement error for each sensor. This clearly assumes that the PD scatter seen in Figs. 1–4 is due to the sensor alone (i.e., the JMR measurement is without error) and thus probably overestimates the sensor error. The main advantage of this approach is to

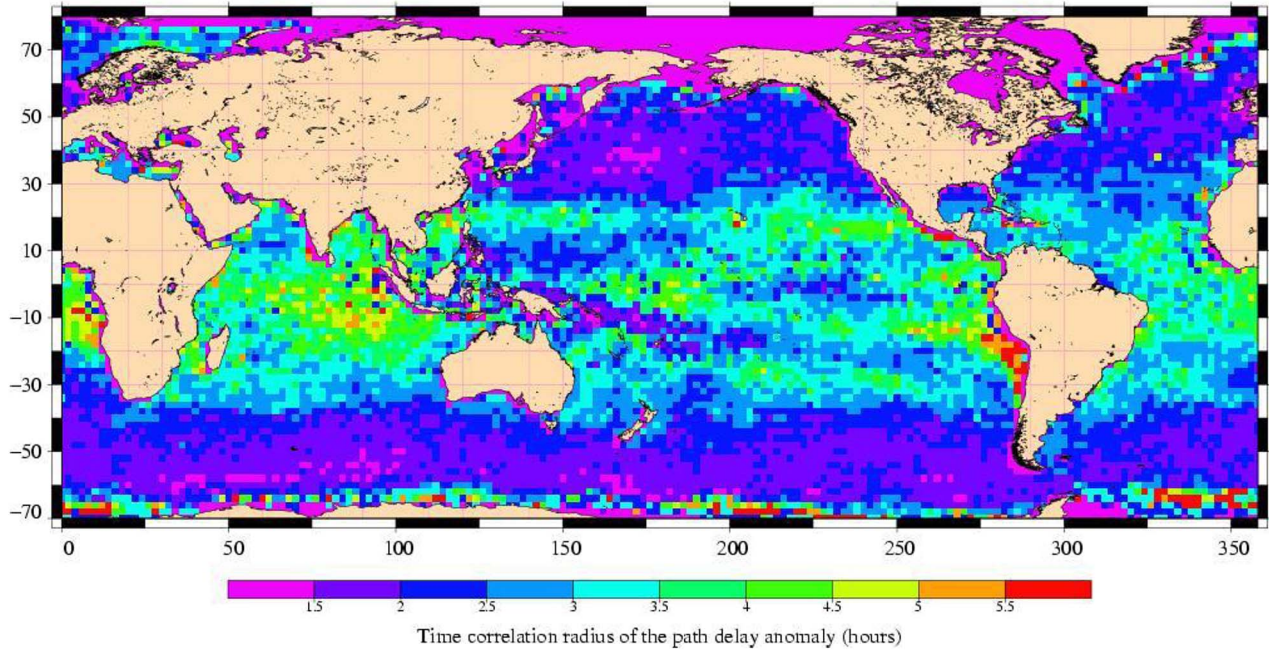


Fig. 8. January mean of the time correlation radius of the PD anomaly in hours. Color scale is from (left) 1.5 h to (right) 5.5 h.

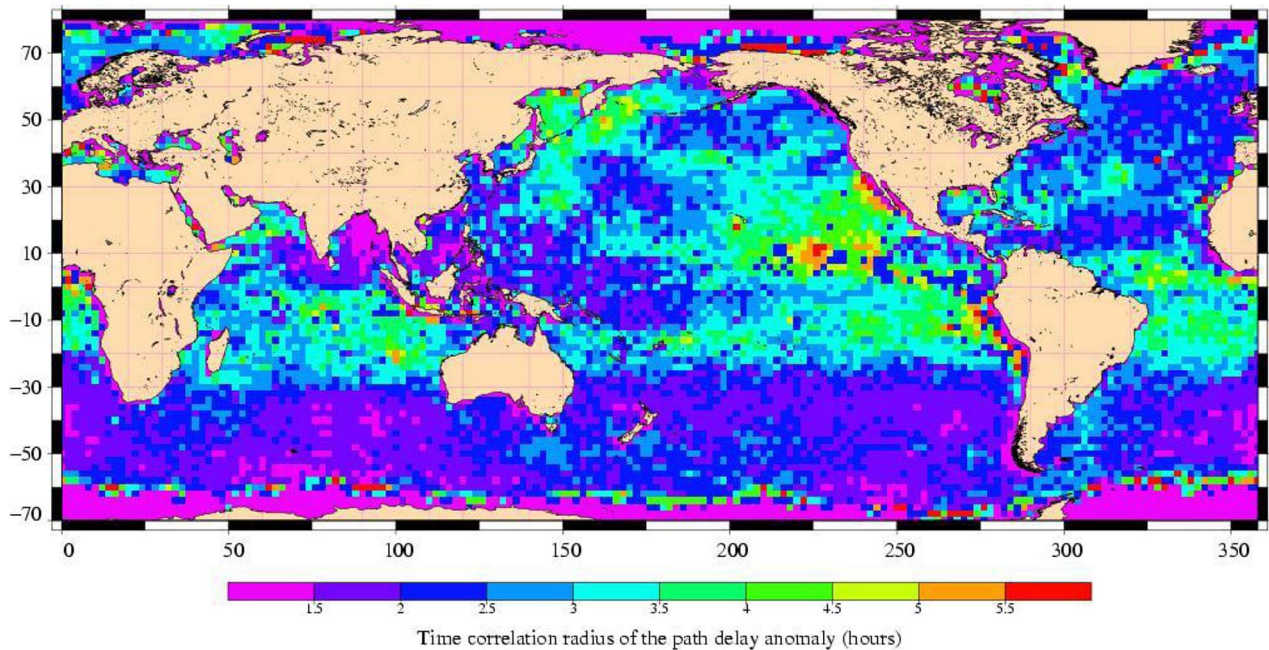


Fig. 9. Same as Fig. 8 except that it is for July.

provide consistent numbers (the same reference data set for all sensors), establishing a sensor error variance ranking from the most accurate (AMSR-E) to the least accurate (AMSU-15). In the OA, this gives more weight to the AMSR-E compared to the AMSU.

C. Building a PD Anomaly Data Set

To compute the variance and correlation function of the field of the PD anomaly, it is first necessary to build a long time series of PD anomaly. The one-year product data set has

been used together with the ECMWF Gaussian grids to build hourly maps of PD anomalies (sensor–ECMWF) at a 0.25° grid resolution. As an example, Fig. 5 shows the PD anomaly map for January 1 between the 3h and 4h UTC. The eight sensors are present and contribute each to the hourly geographic coverage: the large swaths of the five AMSUs, the medium swaths of the SSMI and the AMSR-E, and the smallest low inclination swath of the TMI. The combination of the eight sensors allows a complete ocean coverage in about 4 to 5 h. PD anomalies vary rapidly in space. If we assume that the sensor PD is correct, then this depicts the error of the ECMWF

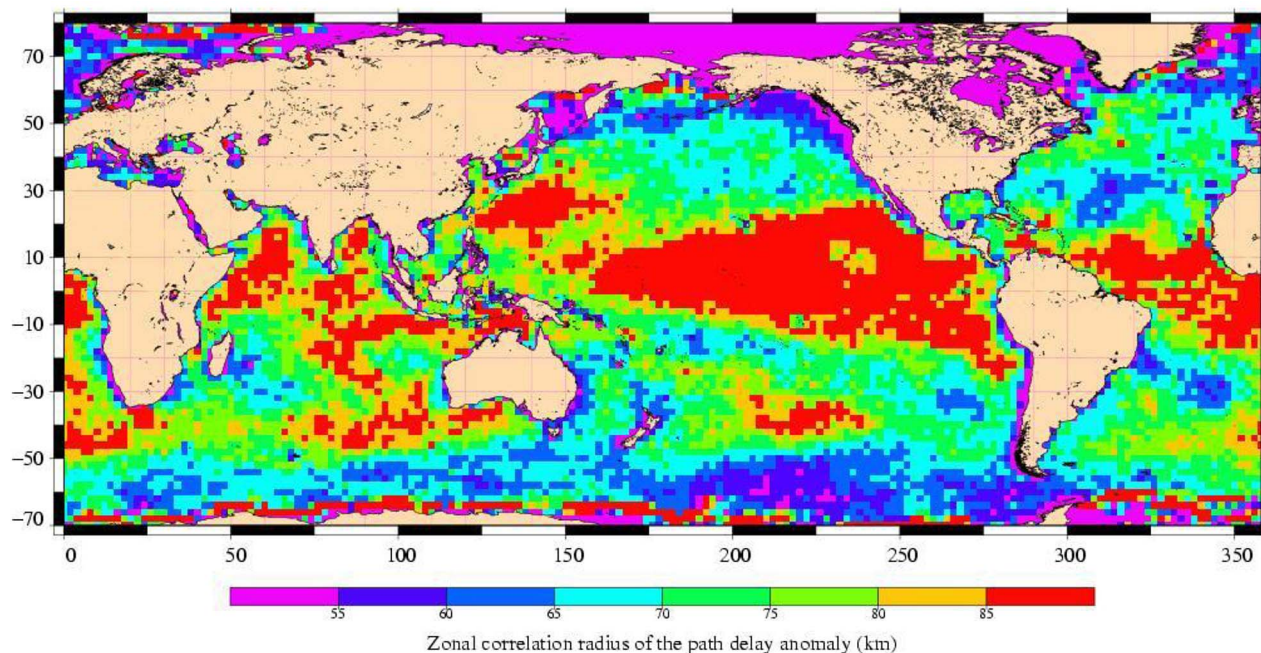


Fig. 10. January mean of the zonal correlation radius of the PD anomaly in kilometers. Color scale is from (left) 55 km to (right) 85 km.

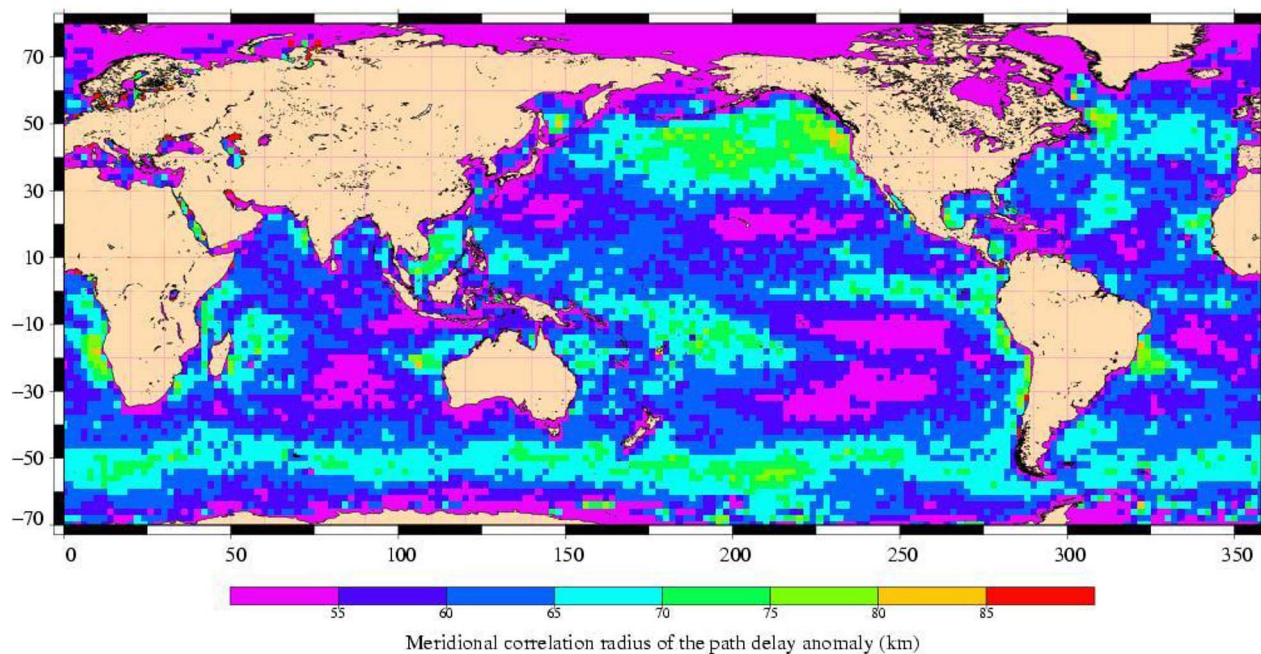


Fig. 11. January mean of the meridional correlation radius of the PD anomaly in kilometers. The same color scale as that for Fig. 10.

model-derived PD. This error is due both to the intrinsic inaccuracy of the ECMWF model to map the humidity field and to its poor temporal resolution (one model output every 6 h).

D. Signal Variance

It is necessary to compute the temporal variance of the field of the PD anomaly over a few hours (timescales of atmospheric humidity) and to characterize the geographical dependence and the seasonal variations of this variance. To obtain a statistically meaningful signal variance in practice, sets of 12 consecutive

PD hourly maps are used to estimate the 12-h variance in $2^\circ \times 2^\circ$ geographical cells, and the variance results are averaged on a monthly basis. Fig. 6 shows the variance map obtained for January. As expected, low signal variance (less than 50 mm^2) is observed in the areas of atmospheric subsidence or low water vapor content. The Pacific and Atlantic zonal circulation areas exhibit medium variance values, and the highest variance values (more than 250 mm^2) are found in the vicinity of the Intertropical Convergence Zone (ITCZ) and South Pacific Convergence Zone, where the PD values are high and often poorly mapped by the model. Fig. 7 shows the variance map obtained for July.

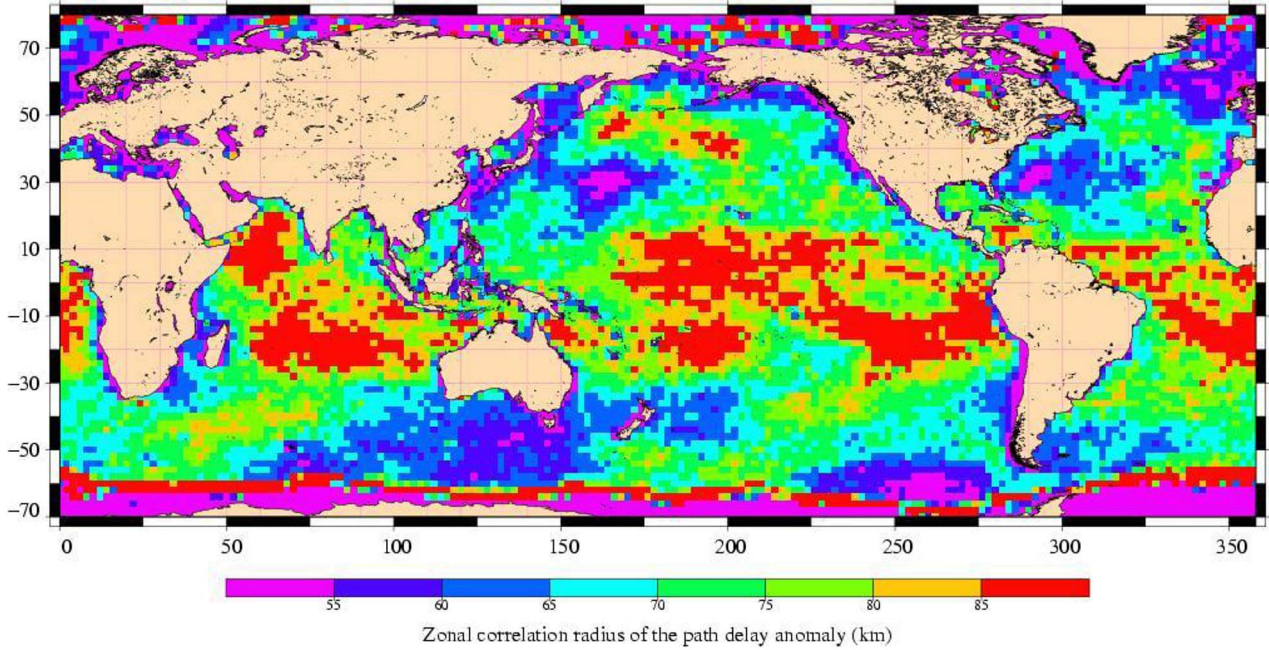


Fig. 12. Same as for Fig. 10 except that it is for July.

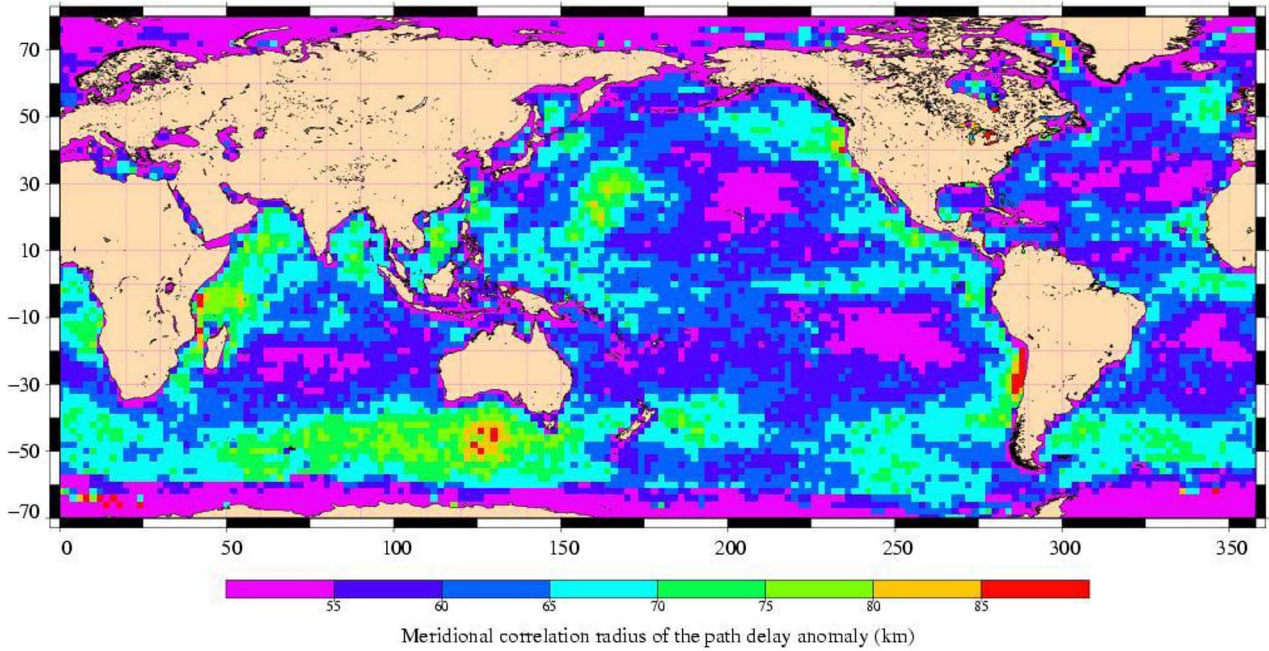


Fig. 13. Same as for Fig. 11 except that it is for July.

Compared to January, the signal variance generally is increased in the Northern Hemisphere and decreased in the Southern Hemisphere, and the values can vary by a factor of two in some places.

E. Correlation Function of the Field of PD Anomaly

As no analytical model of the correlation function of the field of the PD anomaly is available in the literature, a simple Gaussian function has been chosen

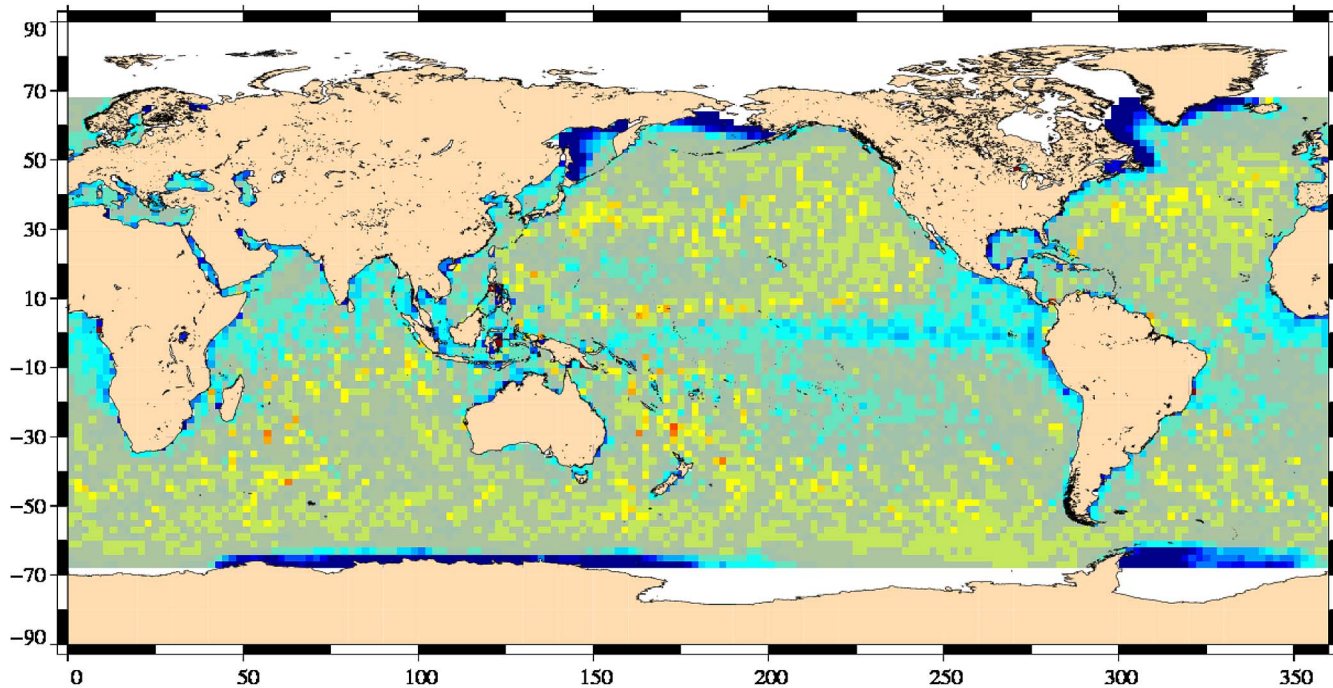
$$\text{CorAno}(x, y, t) = \exp\left(-\frac{x^2}{R_x^2}\right) \exp\left(-\frac{y^2}{R_y^2}\right) \exp\left(-\frac{t^2}{R_t^2}\right) \quad (12)$$

TABLE II
PERCENTAGE OF ALTIMETER POINTS WITH OA-DERIVED PD (WITH FORMAL ERROR < 1) AS FUNCTION OF JASON-1 CYCLE NUMBER

Cycle number	221	222	223	224	225	226
Percentage	84	85	96	94	87	93
Cycle number	227	228	229	230	231	232
Percentage	95	92	101	103	102	96

where x is the zonal distance, y is the meridional distance, t is the time lag from point P where the estimation is done, and R_x , R_y , and R_t are the corresponding

TRO_HUM_OA – TRO_HUM_RAD mean differences
Mission : J1, cycle 221 to 232



TRO_HUM_ECMWF_G – TRO_HUM_RAD mean differences
Mission : J1, cycle 221 to 232

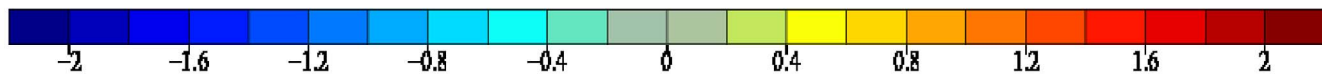
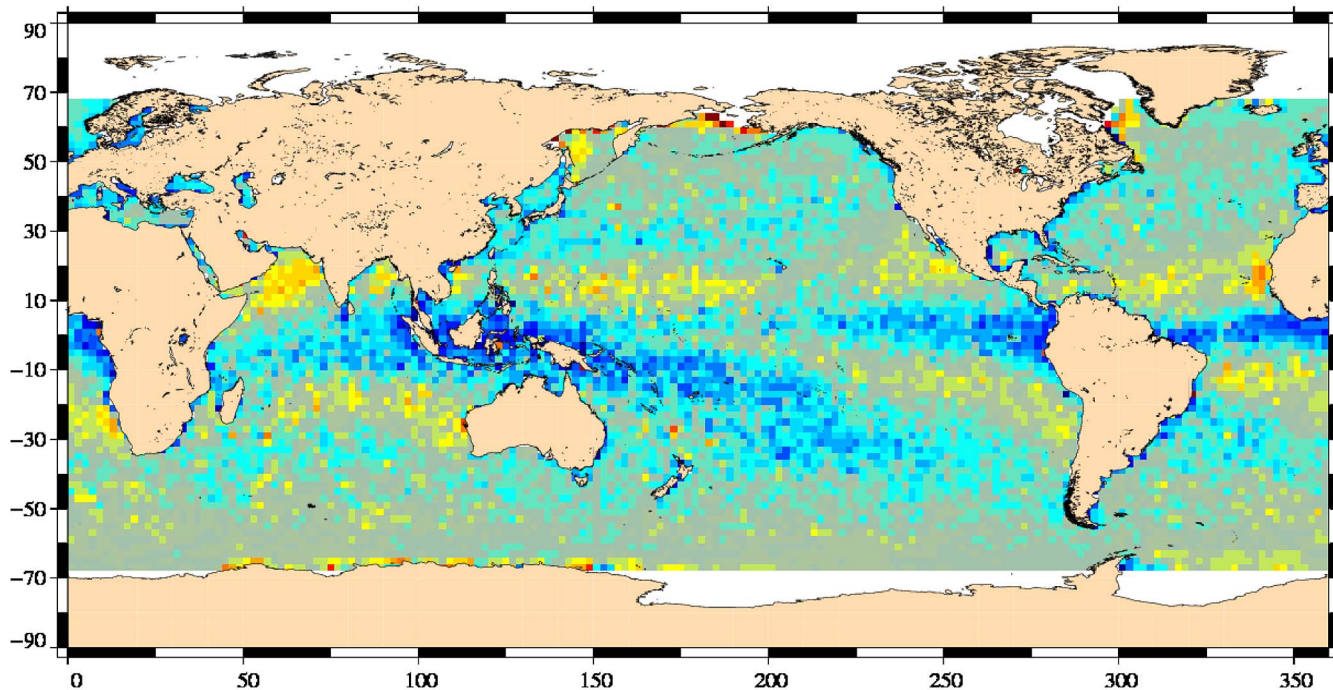
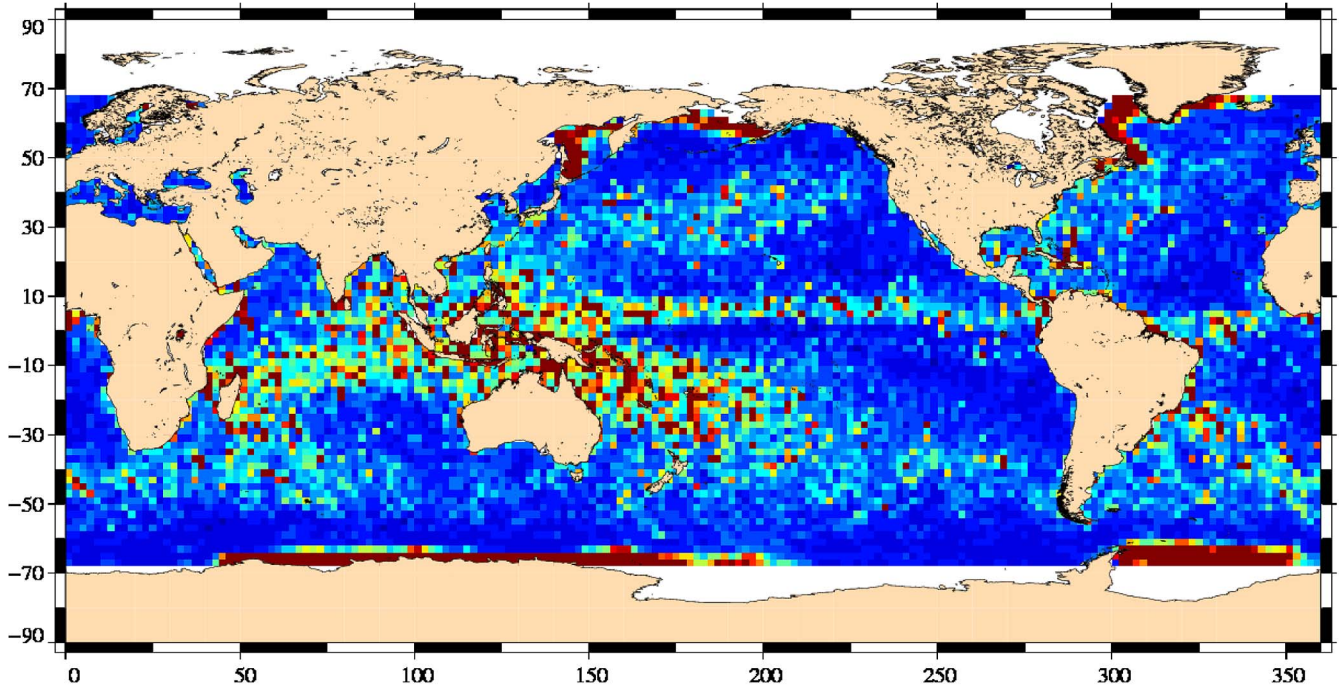


Fig. 14. Mean of (top) the (JMR–OA) PD difference and (bottom) the (JMR–ECMWF) PD difference in centimeters for the Jason-1 12-cycle period.

VAR(TRO_HUM_OA - TRO_HUM_RAD)
Mission : J1, cycle 221 to 232



VAR(TRO_HUM_ECMWF_G - TRO_HUM_RAD)
Mission : J1, cycle 221 to 232

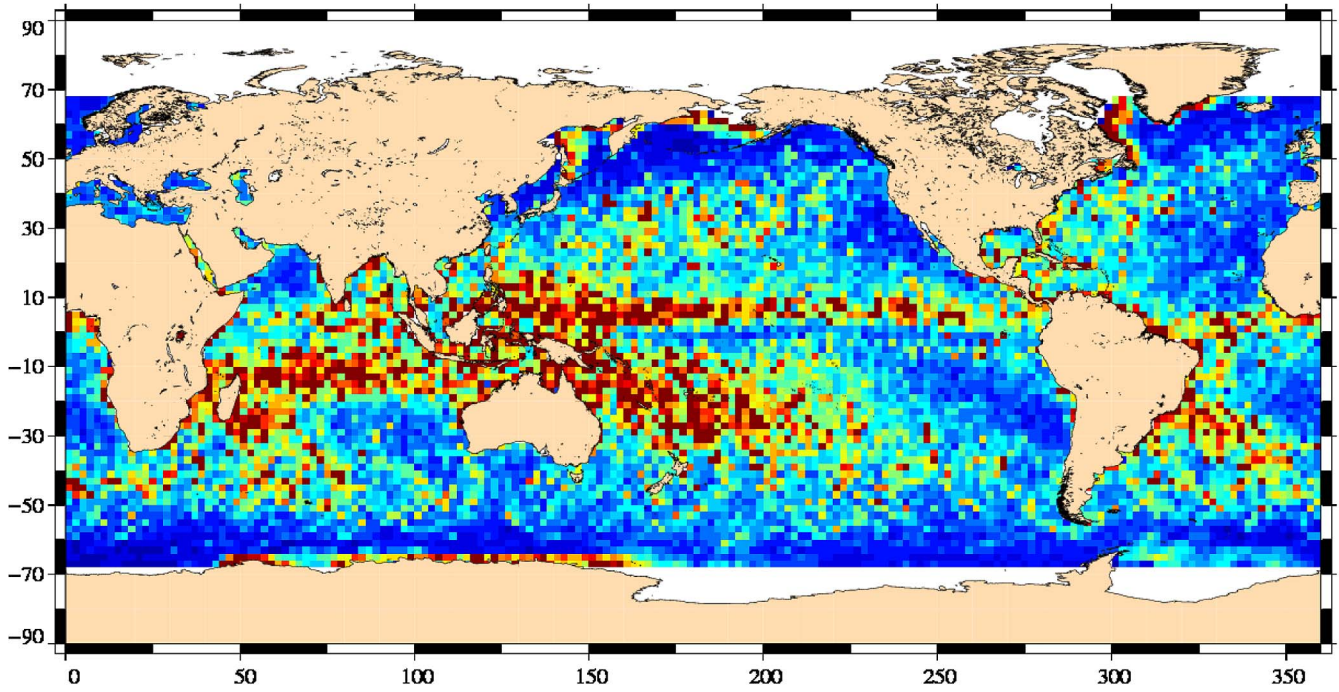


Fig. 15. Variance of (top) the (JMR-OA) PD difference and (bottom) the (JMR-ECMWF) PD difference in square centimeters for the Jason-1 12-cycle period.

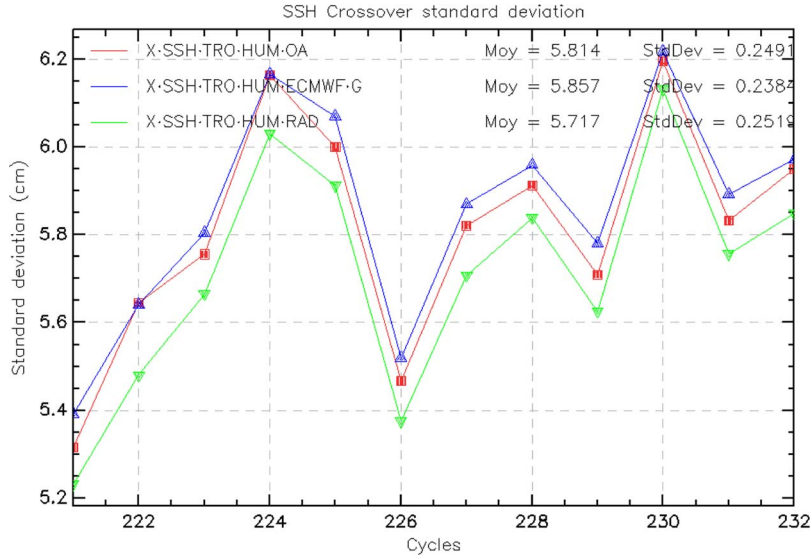


Fig. 16. Standard deviation of the crossover SSH differences (cm), as function of Jason-1 cycle number, for the three PD corrections (JMR, OA, and ECMWF). Moy and StdDev refer to the mean and standard deviation of the crossover SSH differences standard deviation over the 12 cycles.

correlation radii. The calculation of the correlation function is thus restricted to the calculation of the correlation radii.

1) *Time Correlation Radius*: Series of maps of the time correlation coefficient between two PD anomaly maps separated by a given ΔT time interval have first been computed in $2^\circ \times 2^\circ$ cells for different values of ΔT (between 1 and 6 h). Then, the time correlation radius map is simply derived from the series of correlation coefficient maps by finding the corresponding e -folding time ΔT leading to a correlation coefficient of $1/e$. Fig. 8 shows the map obtained for January. The main feature is the contrast between the regions where zonal circulation dominates, characterized by small time correlation radii (less than 2 h), and low-latitude regions with higher correlation radii (up to 5 h), with some exceptions like the southern branch of the ITCZ, where low correlation radius prevails. An arbitrary low (0.5 h) time correlation radius has been assigned to regions where no radiometer measurements are available (e.g., ice-covered polar oceans). Fig. 9 shows the map obtained for July. The seasonal change is noticeable through the northward extension of the small time correlation radii in the Southern Hemisphere (enhanced zonal circulation due to the winter season) and the corresponding increase of the correlation radii in the Northern Pacific and Atlantic (summer season).

2) *Spatial Correlation Radii*: The derivation for spatial correlation radii is similar to that for the temporal radii. First, the zonal and meridional correlation coefficients of the PD anomaly field R_x and R_y have been computed in $2^\circ \times 2^\circ$ cells for different values of zonal and meridional distances Δx and Δy (between 25 and 100 km). Then, the zonal and meridional correlation radii are deduced from the series of correlation coefficient maps by finding the corresponding e -folding distance Δx or Δy leading to a correlation coefficient of $1/e$. Figs. 10 and 11 show the January mean of the zonal and meridional correlation radii, respectively. The values range

from less than 55 km to more than 85 km. The zonal radii are generally greater than the meridional ones. In some areas (e.g., Equatorial Pacific), low meridional radii coincide with high zonal radii. Figs. 12 and 13 show the July zonal and meridional radii, respectively. The same patterns already seen in January are observed, and seasonal variations seem less pronounced.

The OA estimates the PD at a given point P from a subset of radiometer observations $F_i(x, y, t)$ present in a small subdomain around P . The F_i of this subset, by definition, satisfies the following equation:

$$\frac{x^2}{R_x^2} + \frac{y^2}{R_y^2} + \frac{t^2}{R_t^2} \leq 1. \quad (13)$$

From Figs. 10 and 11, one can deduce that the size and eccentricity of the ellipse-shaped subdomain will thus be strongly dependent on the geographic position.

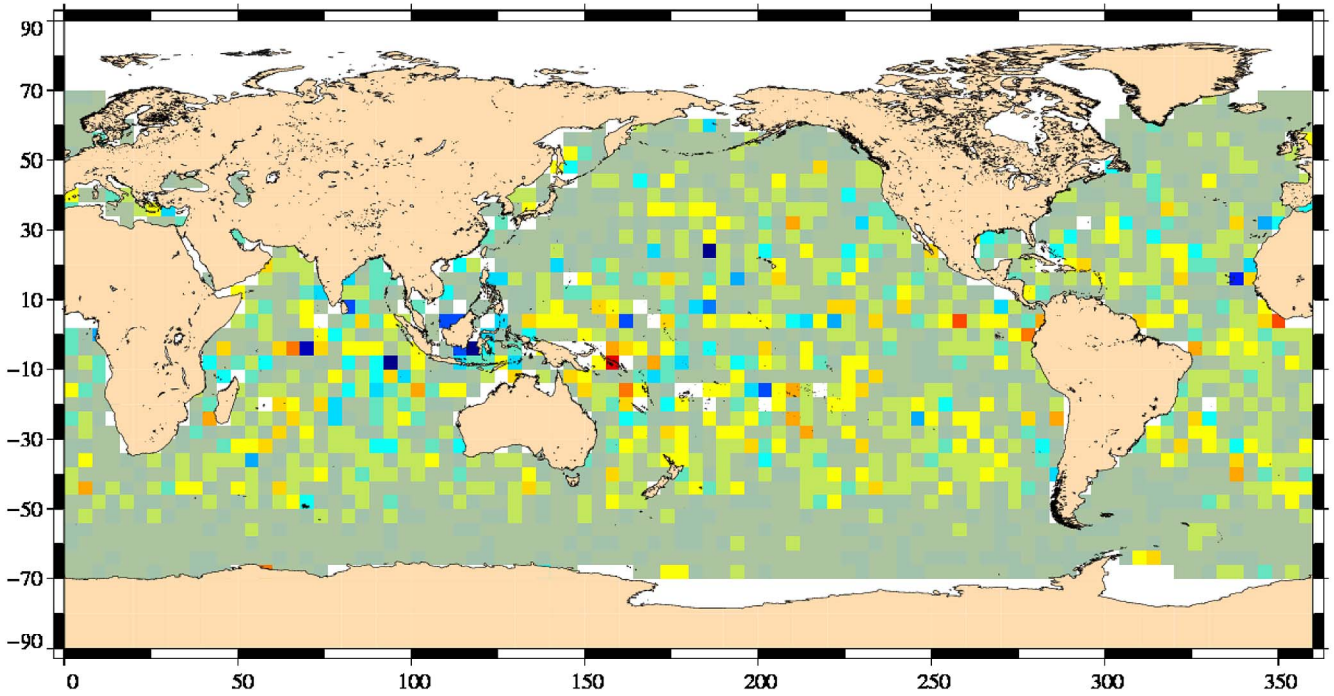
IV. VALIDATION

OA has been used to compute the water vapor PD under the altimeter tracks of Jason-1 cycles 221 to 232, corresponding to the first four months of 2008. The new OA-derived PD (with a formal error < 1) is compared to the JMR and ECMWF PDs.

A. Coverage of the OA-Derived PD

Table II gives for each cycle the ratio of the number of altimeter points with an OA-derived PD, relative to the number of altimeter points with a valid JMR PD, in percent. One factor explaining the disparity of the percentages is the difference in the phasing of the sun-synchronous sensor orbits with the non-sun-synchronous Jason-1 orbit [9], [10]. Some cycles have a more than 100% percentage because altimeter points where the JMR PD is locally not valid (e.g., due to rain contamination)

$\text{VAR}(X_SSH \text{ with TRO_HUM_OA}) - \text{VAR}(X_SSH \text{ with TRO_HUM_RAD}) \text{ norm}$
Mission : J1, cycle 221 to 232



$\text{VAR}(X_SSH \text{ with TRO_HUM_ECMWF_G}) - \text{VAR}(X_SSH \text{ with TRO_HUM_RAD}) \text{ norm}$
Mission : J1, cycle 221 to 232

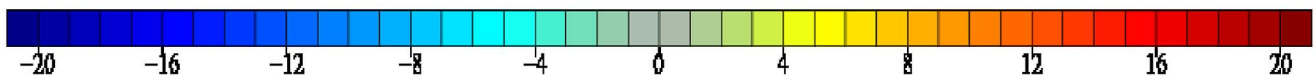
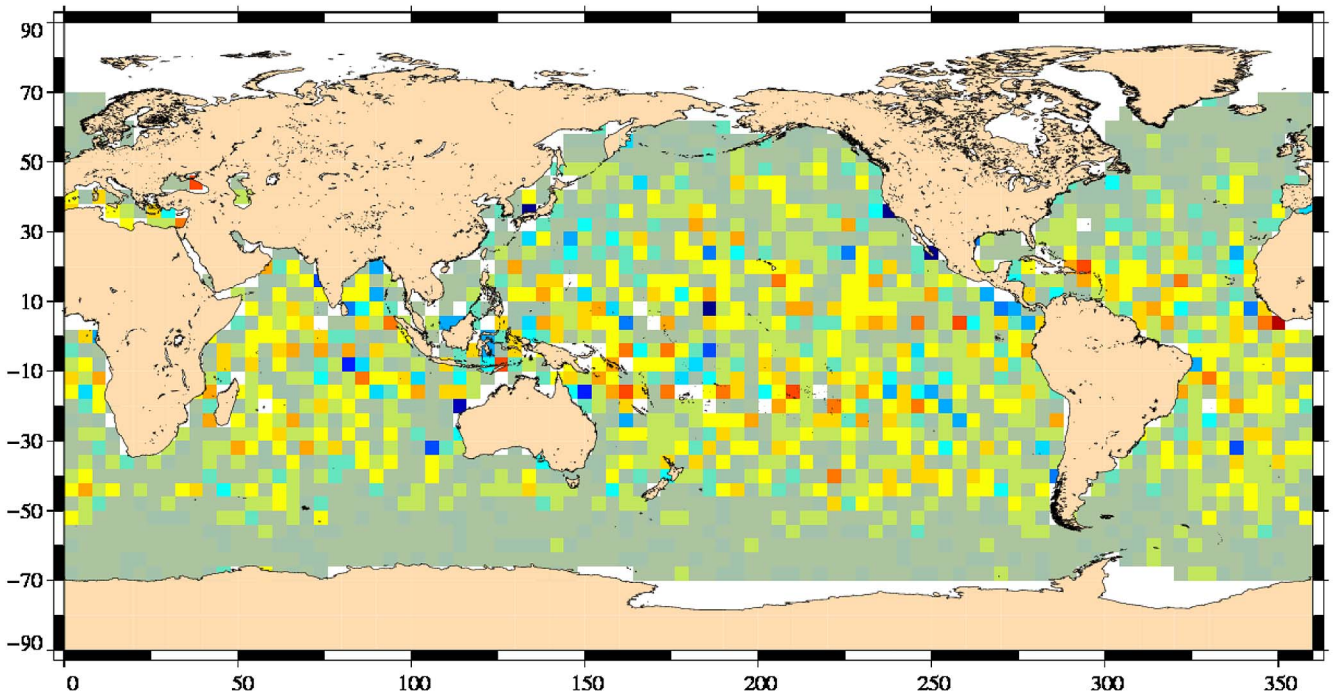


Fig. 17. Relative variation of the variance of the crossover SSH differences (in percent) by using the (top) OA PD correction or (bottom) ECMWF PD correction. Positive values associated with less accurate PD correction are more pronounced with the ECMWF than with the OA.

are filled in with OA PD (which considers the radiometer measurements around).

B. Statistical Comparison of the Three PD Corrections

Maps of the mean of the (JMR–OA) PD difference and the (JMR–ECMWF) PD difference for the 12-cycle period are shown in Fig. 14. There is almost no bias between the OA and JMR PDs in open ocean, but there is some bias (about 1–2 cm) in the areas covered by sea ice. The OA PD is less biased than the ECMWF PD in tropical areas. The corresponding maps of the variance of these differences are shown in Fig. 15. The variance of the (JMR–OA) PD difference is also lower than that of the (JMR–ECMWF) PD difference. This statistical comparison shows that the OA PD correction is closer to that of the JMR than the ECMWF one.

C. SSH Performance Analysis

Altimeter sea surface height (SSH) has been computed as done in [11] using water vapor PD correction from the JMR, ECMWF, and OA. Fig. 16 shows the standard deviation of the SSH differences at Jason-1 crossovers, as a function of the cycle number. As expected, the JMR PD correction (downward triangles) leads to the lowest standard deviation. The OA-derived PD correction (squares) performs better than the ECMWF PD correction (upward triangles).

The performance of the PD corrections can also be quantified by computing the relative increase (or decrease) of the variance of crossover SSH differences G , e.g., for the OA

$$G_{OA} = (\text{Var}(\Delta SSH_{OA}) - \text{Var}(\Delta SSH_{JMR})) / \text{Var}(\Delta SSH_{JMR}) \quad (14)$$

where ΔSSH_{OA} denotes the difference in the SSH computed with the OA-derived PD correction, ΔSSH_{JMR} denotes the difference in the SSH computed with the JMR PD correction, and $\text{Var}()$ is the variance operator.

Fig. 17 shows the map of G_{OA} (top) and the map of G_{ECMWF} (bottom). The variance increase is higher for the ECMWF compared to the OA, mainly in high water vapor content areas, and confirms that the OA PD correction performs better than the ECMWF one.

A similar variance analysis of the SSH differences has been performed using sea level anomalies of the same Jason-1 passes of consecutive cycles, leading to the same results.

V. CONCLUSION

This paper has shown that it is possible to compute a water vapor PD correction for altimetry, with better quality than the one derived from the ECMWF model, by using OA of measurements from all existing scanning radiometers. It is clear that the quality of this new correction depends on the number of available sensors, as well as on their intrinsic accuracy. The OA allows one to optimally combine their measurements but

requires a good *a priori* knowledge of the sensors error and of the statistical properties of the field of the (sensor–ECMWF) PD anomalies to be analyzed. Rough estimates of the sensor errors have been used in this paper, and these need to be improved (e.g., computing geographical maps of the sensors error). The covariance model of the PD anomalies also should be improved through a more realistic correlation function and variance calculation. Although the JMR PD correction remains the most accurate correction for Jason-1, its long-term stability is problematic at the level of accuracy required by sea level rise monitoring: The use of an alternate PD correction, such as the one described in this paper, could thus be valuable. Its application to altimeter missions with no radiometer on board, like the Cryosat-2 mission, is also of high interest for ocean applications.

ACKNOWLEDGMENT

This paper has been carried out in the frame of the Centre National d'Etudes Spatiales Research and Technology Program. The authors would like to thank all data providers, particularly the CLASS staff who kindly accepted to prepare the unusual one-year bulk data orders for the AMSU and the SSM/I.

REFERENCES

- [1] J. Stum, "A comparison between TOPEX microwave radiometer, ERS 1 microwave radiometer, and European Centre for Medium-Range Weather Forecasting derived wet tropospheric corrections," *J. Geophys. Res.*, vol. 99, no. C12, pp. 24 927–24 939, Dec. 1994.
- [2] S. J. Keihm, M. A. Janssen, and C. S. Ruf, "TOPEX/Poseidon microwave radiometer (TMR): III. Wet troposphere range correction algorithm and pre-launch error budget," *IEEE Trans. Geosci. Remote Sens.*, vol. 33, no. 1, pp. 147–161, Jan. 1995.
- [3] S. J. Keihm, V. Zlotnicki, and C. S. Ruf, "TOPEX microwave radiometer performance evaluation, 1992–1998," *IEEE Trans. Geosci. Remote Sens.*, vol. 38, no. 3, pp. 1379–1386, May 2000.
- [4] F. P. Bretherton, R. E. Davis, and C. B. Fandry, "A technique for objective analysis and design of oceanographic experiments applied to MODE-73," *Deep-Sea Res.*, vol. 23, no. 7, pp. 559–582, Jul. 1976.
- [5] R. W. Reynolds and T. M. Smith, "Improved global sea surface temperatures analyses," *J. Clim.*, vol. 7, no. 6, pp. 929–948, Jun. 1994.
- [6] P. Y. Le Traon, F. Nadal, and N. Ducet, "An improved mapping method of multisatellite altimeter data," *J. Atmos. Ocean. Technol.*, vol. 15, no. 2, pp. 522–534, Apr. 1998.
- [7] C. Pottier, V. Garçon, G. Larnicol, J. Sudre, P. Schaeffer, and P. Y. Le Traon, "Merging SeaWiFS and MODIS/Aqua ocean color data in North and Equatorial Atlantic using weighted averaging and objective analysis," *IEEE Trans. Geosci. Remote Sens.*, vol. 44, no. 11, pp. 3436–3451, Nov. 2006.
- [8] S. Brown, C. Ruf, S. Keihm, and A. Kitiyakara, "Jason microwave radiometer performance and on-orbit calibration," *Mar. Geod.*, vol. 27, no. 1/2, pp. 199–220, Jan.–Jun. 2004.
- [9] J. Stum, "A comparison of the brightness temperatures and water vapor path delays measured by the TOPEX, ERS-1, and ERS-2 microwave radiometers," *J. Atmos. Ocean. Technol.*, vol. 15, no. 4, pp. 987–994, Aug. 1998.
- [10] V. Zlotnicki and S. D. Desai, "Assessment of the Jason microwave radiometer's measurement of wet tropospheric path delay using comparisons to SSM/I and TMI," *Mar. Geod.*, vol. 27, no. 1/2, pp. 241–253, Jan.–Jun. 2004.
- [11] J. Dorandeu, M. Ablain, Y. Faugère, F. Mertz, B. Soussi, and P. Vincent, "Jason-1 global statistical evaluation and performance assessment: Calibration and cross-calibration results," *Mar. Geod.*, vol. 27, no. 3/4, pp. 345–372, Jul.–Dec. 2004.



Jacques Stum received the “thèse de 3^{ème} cycle” in atmospheric physics from the University of Clermont-Ferrand, Clermont-Ferrand, France, in 1985.

From 1985 to 1989, he was an Engineer with the Groupement pour le Développement de la Télé-détection Aérospatiale, Toulouse, France, where he worked on the European Remote Sensing satellite (ERS)-1 altimeter and microwave radiometer data processing. Since 1990, he has been with Collecte Localisation Satellites (CLS), Ramonville, France,

where he has been involved in various satellite altimetric missions like ERS-2, TOPEX/Poséidon, Envisat, and Jason-1, working on altimeter and microwave radiometer data processing, validation, and long-term monitoring. Since 2002, he has been in charge of the sea surface temperature and ocean color data processing in CLS. His fields of interest include the satellite data processing of various sensors and platforms, from the telemetry to geophysical parameters, and also the calculation of global near-real-time value-added products for ocean modeling and institutional or private users.



Philippe Sicard received the Engineering degree in computer science from the Ecole Nationale Supérieure de Mécanique of Nantes, Nantes, France, in 1980.

He is currently with Collecte Localisation Satellites (CLS), Ramonville, France, where he was with the Space Oceanographic Division in 1992 working on various projects and studies first as a Software Engineer and then as a Technical Manager. Since 2010, he has been with the Technical Division, CLS, where he was appointed the Head of the “Scientific

Software” Department.



Loren Carrère received the Ph.D. degree in physical oceanography from the Paul Sabatier University, Toulouse, France, in 2003.

Since 2003, she has been with Collecte Localisation Satellites, Ramonville, France, in the department of validation and valorization of altimetric data. She has been involved in various satellite altimetric missions like TOPEX/Poséidon, Envisat, Jason-1, and Jason-2, working on the improvement of geophysical and instrumental corrections, on the development of the dynamic atmospheric correction’s model, on

coastal products, and on different studies based on altimetric data. She also participates in the definition of new orbits for future reference altimeter missions. Other fields of interest include the development of new altimeter products for ocean applications and the development of high-frequency modeling for several applications.

Juliette Lambin received the Engineering degree from Ecole Polytechnique, Palaiseau, France, in 1997, and the Ph.D. degree in geophysics from the Institut de Physique du Globe de Paris, Paris, France, in 2001.

From 2001 to 2005, she was a Postdoctoral Fellow with the California Institute of Technology, Pasadena. Since 2005, she has been with the Centre National d’Etudes Spatiales, Toulouse, France, as a Mission Engineer for oceanography, hydrology, and cryosphere.